THE JOURNAL OF PHYSICAL CHEMISTRY C
A JOURNAL OF THE AMERICAN CHEMICAL SOCIETY

pubs.acs.org/JPCC

Article

Tuning Electronic and Magnetic Properties of Monolayer $MnPSe_3$ via Surface Adsorption

Dong Liu, Sike Zeng, Ji-Hai Liao, and Yu-Jun Zhao*

Cite This: *J. Phys. Chem. C* 2025, 129, 17287−17295

Read Online

ACCESS | Metrics & More | Article Recommendations | Supporting Information

ABSTRACT: The engineering of magnetic order and electronic states in two-dimensional (2D) materials is pivotal for advanced spintronic technologies. Despite their potential, the scarcity of intrinsic 2D ferromagnetic and ferrovalley materials remains a critical challenge. Here, we employ density functional theory with Hubbard-*U* corrections to systematically investigate adsorbate-driven magnetic transitions in monolayer $MnPSe_3$. While pristine $MnPSe_3$ exhibits antiferromagnetic (AFM) ordering with a semiconducting gap, Li and F adsorption at coverages of 33−100% induces an AFM-to-ferromagnetic (AFM−FM) transition, whereas only full (100%) O adsorption yields the same magnetic phase change. Our calculations reveal enhanced thermodynamic stability at elevated coverages, with full-coverage configurations ($Li_{0.5}MnPSe_3$, $MnPSe_3O_{0.5}$, $MnPSe_3F_{0.5}$) favored energetically. Hybrid functional (HSE06) calculations show that F adsorption drives a semiconductor-to-half-metal transition, whereas Li and O adsorption preserves the semiconductivity. Moreover, Li adsorption breaks the *MT* symmetry protecting the *K*/*K*′ degeneracy in $MnPSe_3$, and when spin−orbit coupling is included, it induces a 20.3 meV valley splitting in the valence band, thereby rendering $Li_{0.5}MnPSe_3$ an intrinsically valley-polarized FM semiconductor. Crucially, carrier doping results indicate that once the electron doping concentration reaches 8.3×10^{13} cm^{-2}, the magnetic easy axis of monolayer $MnPSe_3$ transitions from in-plane to out-of-plane. This work establishes atomic adsorption as a robust strategy for tailoring 2D magnetism, resolving discrepancies through the rigorous treatment of exchange-correlation effects and configurational diversity.

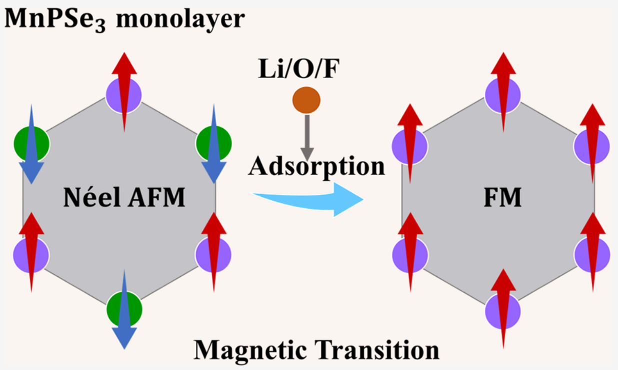

1. INTRODUCTION

Two-dimensional (2D) van der Waals magnetic materials have garnered significant attention in recent years, and the manipulation of their magnetism is essential for understanding their physical properties and realizing their practical applications.[1−3] As stated by the Mermin−Wagner theorem, long-range magnetic order could not exist in 2D isotropic systems at finite temperature due to thermal fluctuation.[4] Therefore, the magnetic anisotropy induced by spin−orbit coupling is essential for maintaining long-range magnetic order in 2D materials. The successful synthesis of 2D ferromagnetic (FM) materials such as $Cr_2Ge_2Te_6$,[5] CrI_3,[6] and Fe_3GeTe_2[7] in experiments has greatly promoted the research of spintronics. Unfortunately, most of the discovered 2D intrinsic FM materials are metallic and unstable under ambient conditions, which has impeded the further advancement of spintronics.[5,6,8]

It is well established that half-metals with one conductive channel and one insulating spin channel, as well as novel van der Waals (vdW) FM semiconductors, have been considered as ideal materials for spintronics applications.[9,10] To this end, the exploration of novel vdW FM half-metals and semiconductors is desired for the realization of 2D spintronic devices.[11,12] The typical approaches to manipulate magnetism in 2D materials is through an electric field, mechanical strain, chemical modification, defect doping, atom adsorption, and magnetic field.[13−19] Among the aforementioned methods for manipulating their magnetic properties, surface functionalization via physical and chemical adsorption is an effective approach owing to the large specific surface area of 2D materials.[20]

Bulk $MnPSe_3$ is a vdW magnetic material, and previous neutron scattering experiments revealed a collinear antiferromagnetic (AFM) order for its layered system.[21] The interlayer spacing between the magnetic atomic layers is about 6.7 Å, making it an ideal candidate for 2D magnetism. Few-layer $MnPSe_3$ has already been synthesized experimentally through mechanical exfoliation.[22] Monolayer $MnPSe_3$, with a Néel-AFM ground state, has been investigated for potential AFM−FM transitions by various methods. For instance, AFM−FM phase transitions can be induced through gate-controlled

Received: June 11, 2025
Revised: August 27, 2025
Accepted: September 2, 2025
Published: September 12, 2025

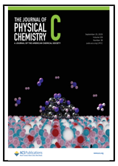

https://doi.org/10.1021/acs.jpcc.5c04044

electron or hole doping.[10,18] Recent studies have demonstrated that by applying a vertical electric field, substituting Se atoms with S to construct a Janus structure, or forming heterostructures with other 2D materials, altermagnetism (AM) can be induced in the monolayer MnPSe$_3$.[23] Moreover, as demonstrated in recent studies,[24,25] spontaneous valley polarization has been successfully achieved in MnPSe$_3$−W Se$_2$ and MnPSe$_3$−Hf N$_2$ heterostructures. Therefore, it is considered to be a highly promising 2D material for spintronic and valleytronic devices. However, as an effective regulation approach, the effect of chemical adsorption on this system has been rarely studied.

In this work, we investigate the effects of Li, O, and F adsorption at varying coverages on the electronic structure and magnetic properties of monolayer MnPSe$_3$. By surveying multiple AFM (stripy, zigzag) configurations, we find that Li and F induce an AFM−FM transition only above 33% coverage, whereas O triggers this transition solely at 100% coverage. Adsorption energies and thermodynamic stability calculations reveal that 100% coverage of Li, O, and F is the most favorable, motivating our detailed focus on these cases. With the consideration of spin−orbit coupling (SOC), hybrid-functional (HSE06) band-structure calculations show that Li adsorption not only preserves a finite band gap but also breaks the K/K' symmetry to induce valley polarization and converts MnPSe$_3$ from an AFM semiconductor to an FM semiconductor—suggesting the simultaneous control of charge, valley, and spin degrees of freedom. O adsorption likewise drives an AFM−FM transition with dramatic band-gap reduction, while F adsorption transforms the system into an FM half-metal. To elucidate the underlying mechanisms, we construct an anisotropic Heisenberg Hamiltonian and perform symmetry analyses that clarify the origin of the magnetic phase transitions and valley polarization. Finally, carrier doping simulations across an expanded set of magnetic configurations demonstrate that an electron density exceeding 8×10^{13} cm^{-2} flips the magnetic easy axis (EA) from in-plane to out-of-plane. Notably, when including additional AFM states, the critical carrier concentration for the AFM−FM transition is higher than previously reported, underscoring the importance of comprehensive magnetic sampling. These findings not only resolve discrepancies in the literature but also establish atomic adsorption as a robust strategy for tailoring spin-ordering and electronic properties in 2D AFM semiconductors, advancing their potential for spintronic and valleytronic applications.

2. COMPUTATIONAL DETAILS

Our calculations are carried out within the Perdew−Burke−Ernzerhof generalized gradient approximation (GGA)[26] implemented in the Vienna ab initio simulation package,[27] along with HSE06 for the band structure.[28] An energy cutoff of 500 eV for the plane waves is adopted. The slab model of the system is constructed using 20 Å vacuum along the [001] direction (i.e., z direction) to prevent periodic image interactions between the neighboring layers. Monkhorst k-mesh grids of $9 \times 9 \times 1$, $6 \times 9 \times 1$, $6 \times 6 \times 1$, and $4 \times 4 \times 1$ are used for Brillouin-zone sampling of $1 \times 1 \times 1$, $2 \times 1 \times 1$, $\sqrt{3} \times \sqrt{3} \times 1$, and $2 \times 2 \times 1$ MnPSe$_3$, respectively. For geometry optimization, all of the internal coordinates are relaxed until the Hellmann−Feynman force is less than 0.01 eV $\cdot$ Å^{-1} for each ion, and the total energy convergence is within 10^{-6} eV. SOC is applied in the calculations of magnetic anisotropic energy (MAE).[29,30] When calculating magnetic properties, the effective Hubbard U correction applied on the 3d electrons of Mn atoms is 4 eV, following a few references.[31−33] Our Néel temperature simulations of pristine monolayer MnPSe$_3$ are carried out using the VAMPIRE atomistic simulation software package.[34,35]

3. RESULTS AND DISCUSSION

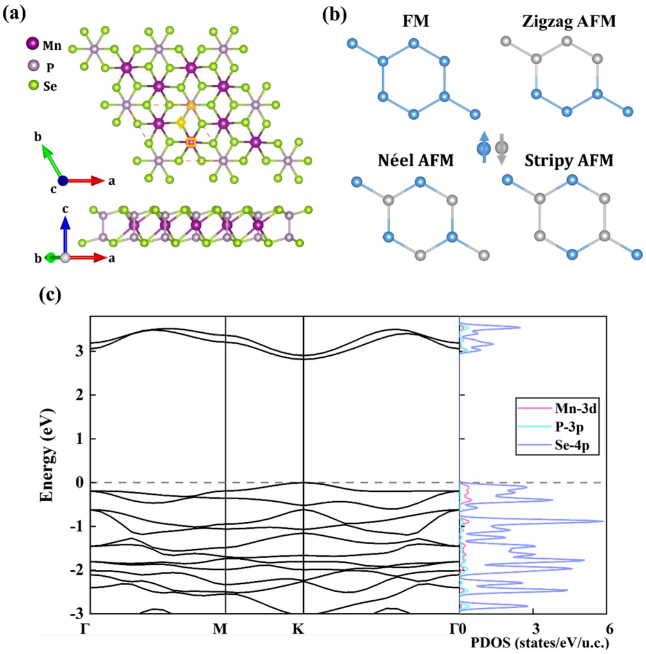

Figure 1. (a) Top and side views of the monolayer MnPSe$_3$, and the area enclosed by the red dashed lines denotes the unit cell, where the square, rhombus, and triangle denote the three considered adsorption sites. (b) Four different magnetic configurations of the FM, zigzag-AFM, Néel-AFM, and stripy-AFM. (c) Band structure and PDOS of monolayer MnPSe$_3$ without SOC, obtained with the HSE06 functional. The blue and gray balls are the spin-up and spin-down state Mn atoms, respectively.

3.1. Geometric, Electronic Structure, and Magnetic Ground State.

The top and side views of the crystal structure of monolayer MnPSe$_3$ are shown in Figure 1a, with the area enclosed by the red dashed lines representing the unit cell. Each unit cell contains two Mn atoms, six Se atoms, and two P atoms. The lattice parameters of the optimized structure are $a = b = 6.457$ Å, in agreement with the recently reported value of $a = b = 6.387$ Å.[16] Clearly, the 2D MnPSe$_3$ layer consists of two Mn^{2+} ions arranged in a hexagonal honeycomb lattice, along with a $[P_2Se_6]^{4-}$ bipyramid, which is formed by a P−P dimer connected to two selenium trimers that vertically pass through the center of each honeycomb plane. To determine the magnetic ground state of 2D MnPSe$_3$, four phases with different magnetic orders—FM, zigzag antiferromagnetic (zigzag-AFM), Néel antiferromagnetic (Néel-AFM), and stripy antiferromagnetic (stripy-AFM)—are constructed using a $2 \times 2 \times 1$ supercell, as shown in Figure 1b. According to our calculations, the Néel-AFM state exhibits the lowest energy among the four phases, while the energy of the FM state is approximately 21.9 meV/formula unit (f.u.) higher, consistent with previous reports.[22,36,37] The local magnetic moment of the Mn atom is about 4.6 μ_B, where Mn possesses about +2e charge with a high-spin state. Projected density of states (PDOS) analysis reveals that electronic states near E_F are dominated by Se-4p orbitals, with minimal P-3p contributions, consistent with the charge-transfer character of the gap.

The well-documented band-gap underestimation inherent to the PBE functional is evident in our calculations, yielding an HSE06 band gap of 2.80 eV for monolayer $MnPSe_3$, which slightly exceeds the previously reported value of 2.56 eV,[38] as shown in Figure 1c. This discrepancy persists even with the inclusion of a Hubbard-U correction (U = 4, 5, and 6 eV), where PBE+U produces gaps of 1.76, 1.87, and 1.93 eV (Figure S1), confirming systematic underestimation across exchange-correlation treatments.

3.2. Thermodynamic Stability of Li_xMnPSe_3, $MnPSe_3O_x$, and $MnPSe_3F_x$.

Subsequently, we systematically investigated stable adsorption sites and magnetic ground states for Li, F, and O adatoms. To model four distinct coverage regimes (25, 33, 50, 100%), we considered single adatom adsorption in four supercell configurations: 1 × 1 × 1, 2 × 1 × 1, $\sqrt{3} \times \sqrt{3} \times 1$, and 2 × 2 × 1, as illustrated in Figure S2. For Li_xMnPSe_3, $MnPSe_3O_x$, and $MnPSe_3F_x$, three adsorption sites were evaluated (Figure 1a): above Mn (square), Se (rhombus), and P (triangle). For each configuration, multiple magnetic orderings were considered—two for 1 × 1 × 1 (FM and Néel-AFM), three for 2 × 1 × 1 and $\sqrt{3} \times \sqrt{3} \times 1$ (FM, Néel-AFM, and zigzag-AFM), and four for 2 × 2 × 1 (FM, Néel-AFM, zigzag-AFM, and stripy-AFM). Our calculations indicate that at 100% coverage, Li adsorption preferentially occupies the Mn site, whereas the O and F atoms favor the P site. The corresponding adsorption energies for each site are listed in Table S1.

However, when lower coverages and additional AFM configurations are considered, Li and F adsorption at 25% coverage only drives the ground state from Néel-AFM to stripy-AFM. The corresponding energy differences ΔE_{AFM-FM} are −16 and −2.4 meV/f.u. for Li and F, respectively, indicating that a true AFM−FM transition does not occur at this coverage. Moreover, for Li adsorption at 33, 50, and 100% coverages, ΔE_{AFM-FM} values are 0.07, 8.0, and 18.4 meV/f.u., respectively. For F adsorption at the same coverages, ΔE_{AFM-FM} values are 5.2, 44.3, and 64.2 meV/f.u., respectively.

For the adsorption of O at 25, 33, and 50% coverages, no AFM−FM transition occurs because the zigzag-AFM configuration remains the lowest-energy state. The energy differences ΔE_{AFM-FM} for O coverages of 25, 33, and 50% are −0.27 meV/f.u., −0.19, and −0.46 eV/f.u., respectively, and the magnetic ground state shifts from the pristine Néel-AFM to zigzag-AFM. We further observe that O adsorption induces substantially larger lattice distortions than Li or F, suggesting that distortion-driven modifications of the magnetic exchange interactions underpin the stabilization of the zigzag-AFM phase.

To verify the feasibility of adsorption, we calculated the adsorption energy for each atom using the following formula:

$$E_{ad} = E_{total} - E_{MnPSe_3} - E_i \tag{1}$$

Here, E_{MnPSe_3} denotes the total energy of the pristine monolayer, E_{total} corresponds to the energy of the adsorbate−substrate system, and E_i represents the energy of an isolated i atom in its free state. As shown in Table 1, the adsorption energies of Li, O, and F on the surface of monolayer $MnPSe_3$ for all four coverages are negative, confirming the feasibility of adsorption. Furthermore, to preclude the formation of bulk elemental phases (e.g., Li-metal, O_2, and F_2), we calculated the cohesive energy $E_{coh} = E_{bulk} - E_{single}$, where E_{bulk} and E_{single} denote the energies of bulk elements and isolated atoms, respectively. The derived values (E_{coh} (Li) = −1.74 eV, E_{coh} (O) = −3.04 eV, and E_{coh} (F) = −1.39 eV) are less negative than the corresponding adsorption energies across all coverage regimes (Table 1). This confirms that Li, O, and F adatoms preferentially stabilize as surface-bound species rather than aggregating into bulk phases under the studied conditions.

Table 1. Adsorption Energies E_{ad} for Li, O, and F Adatoms on Monolayer $MnPSe_3$ across Four Coverage Regimes (25, 33, 50, and 100%)

coverage (eV)	25%	33%	50%	100%
$E_{ad(Li)}$	−2.0	−1.97	−2.16	−2.23
$E_{ad(O)}$	−3.28	−3.76	−3.83	−3.44
$E_{ad(F)}$	−3.21	−3.24	−3.28	−3.32

To assess thermodynamic stability, we first established equilibrium chemical potential constraints for Mn, P, and Se during crystal growth as follows:

$$\Delta\mu_{Mn} + \Delta\mu_P + 3\Delta\mu_{Se} = \Delta H_f(MnPSe_3) \tag{2}$$

where $\Delta H_f(MnPSe_3)$ is the calculated formation energy of $MnPSe_3$. The stable chemical potential range of $MnPSe_3$ is determined by constraining the possible competing phases of Mn, P, and Se. To prevent the formation of binary phases (MnSe, $MnSe_2$, MnP, MnP_2, Mn_3 P, and PSe) and elemental species, the following constraints are imposed on the chemical potentials in this work:

$$\Delta\mu_{Mn} \le 0,\ \Delta\mu_P \le 0,\ \Delta\mu_{Se} \le 0 \tag{3}$$

$$\Delta\mu_{Mn} + \Delta\mu_{Se} \le \Delta H_f(MnSe) \tag{4}$$

$$\Delta\mu_{Mn} + 2\Delta\mu_{Se} \le \Delta H_f(MnSe_2) \tag{5}$$

$$\Delta\mu_{Mn} + \Delta\mu_P \le \Delta H_f(MnP) \tag{6}$$

$$\Delta\mu_{Mn} + 2\Delta\mu_P \le \Delta H_f(MnP_2) \tag{7}$$

$$3\Delta\mu_{Mn} + \Delta\mu_P \le \Delta H_f(Mn_3P) \tag{8}$$

Phase diagrams of the Mn−P−Se system under equilibrium conditions were computed by evaluating competing binary phases, yielding permissible chemical potential ranges (blue region in Figure 2a). Thus, we obtain the chemical potential ranges of Mn, P, and Se in $MnPSe_3$: $-2.49 \le \Delta\mu_{Mn} \le -1.74$; $-0.60 \le \Delta\mu_P \le 0$; $-0.30 \le \Delta\mu_{Se} \le 0$ (eV). Building on these constraints and incorporating electronegativity considerations, we derived phase diagrams for Li−P−Se, Mn−O, and Mn−F systems (Figure 2b−d), determining the stable chemical potential windows for Li, O, and F adsorption (blue regions).

As the adsorption energy E_{ad} is consistent with the chemical potential $\Delta\mu$ for the adsorbate, the comparison of coverage-dependent chemical potentials (Table 1) with this stability confinement demonstrates that Li_xMnPSe_3 and $MnPSe_3O_x$ remain stable across all four coverages. However, $MnPSe_3F_x$ configurations exhibit inherent thermodynamic instability in Mn-rich/F-poor conditions (Figure 2c), achieving stability only when $\Delta\mu_{Mn} < -2.20$ eV. Notably, increasing Li and F

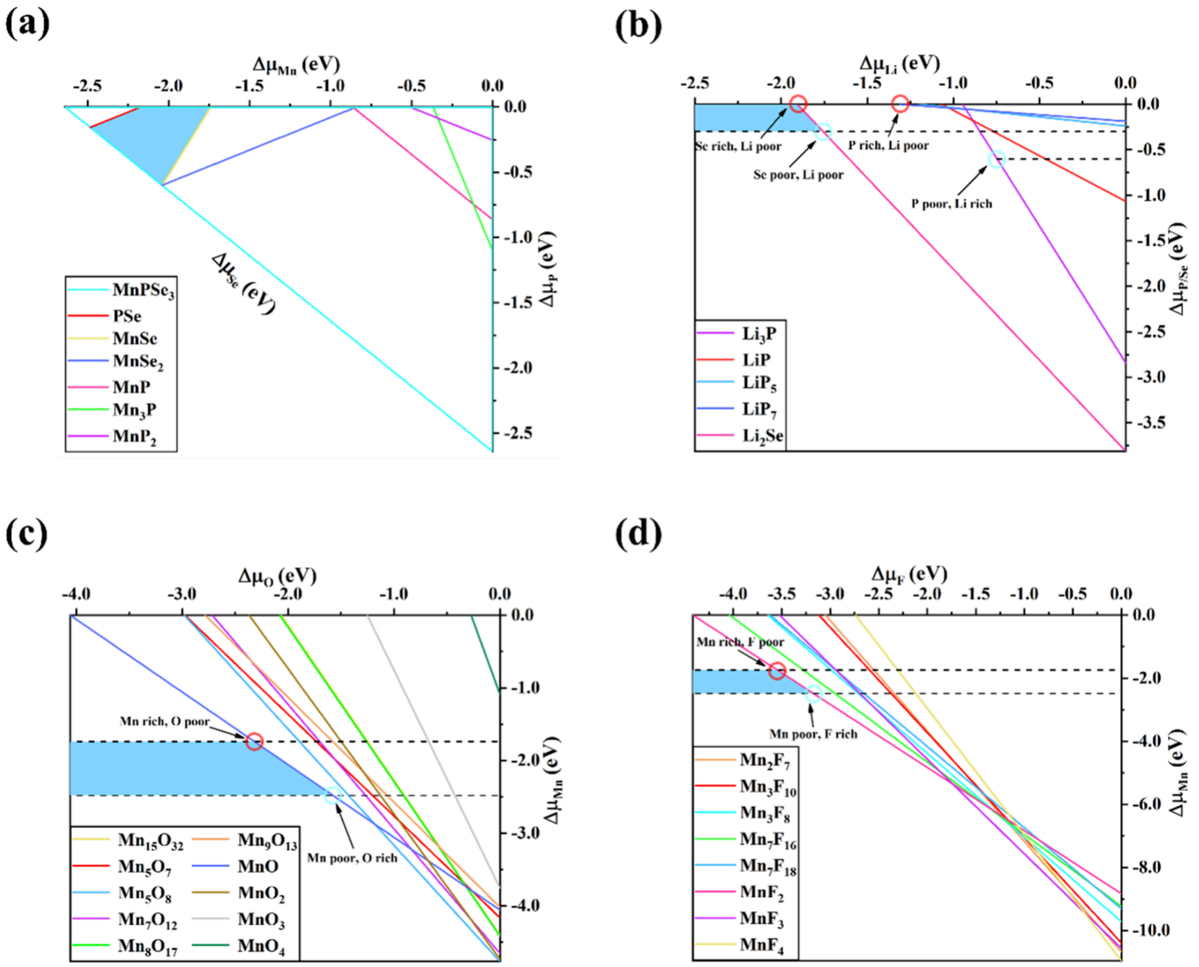

Figure 2. (a) Parametrized phase diagram of $MnPSe_3$ projected onto the ($\Delta\mu_{Mn}$, $\Delta\mu_P$) plane. The blue region denotes the thermodynamically permissible range of Mn, P, and Se chemical potentials under equilibrium conditions. (b) Li−P−Se phase diagram constrained by the permissible $\Delta\mu_P$ and $\Delta\mu_{Se}$ ranges. The blue region defines stable Li chemical potentials ($\Delta\mu_{Li}$). (c) Mn−O phase diagram under the equilibrium $\Delta\mu_{Mn}$ constraint. The blue region indicates stable $\Delta\mu_O$ values. (d) Mn−F phase diagram within the equilibrium $\Delta\mu_{Mn}$ range. The blue region marks permissible $\Delta\mu_F$ values.

adsorption coverage induces progressive shortening of adatom-surface bond lengths, indicative of enhanced interfacial bonding at higher adsorption densities. In contrast, O adsorption exhibits minimal bond-length variation across coverage regimes. This behavior partially explains the anomalous trend observed in Table 1, where higher coverages of Li and F correspond to more negative adsorption energies. Moreover, the low-coverage adsorption configurations of Li, O, and F are intrinsically unstable and tend to coalesce into locally dense regions. Consequently, we restricted our subsequent analyses of magnetic and electronic properties to full-coverage systems ($Li_{0.5}MnPSe_3$, $O_{0.5}MnPSe_3$, and $F_{0.5}MnPSe_3$).

3.3. Electronic Properties of $Li_{0.5}MnPSe_3$, $MnPSe_3O_{0.5}$, and $MnPSe_3F_{0.5}$. To investigate the electronic structures of $Li_{0.5}MnPSe_3$, $MnPSe_3O_{0.5}$, and $MnPSe_3F_{0.5}$, we calculated the corresponding band structures (Figure 3d−f) by using the HSE06 method. As shown in Figure 3d,e, upon adsorption of Li and O atoms, the monolayer $MnPSe_3$ transitions from an AFM semiconductor to an FM semiconductor, with the corresponding band gaps decreasing by approximately 2.1 and 2.7 eV, respectively. In contrast, the adsorption of the F atom transforms the system into an FM half-metal, as shown in Figure 3f.

Additionally, we calculated the band structures of $Li_{0.5}MnPSe_3$ and $O_{0.5}MnPSe_3$ using the PBE+U (U = 4 eV) method for comparison (see Figure S3). The resulting band structures indicate that both $Li_{0.5}MnPSe_3$ and $O_{0.5}MnPSe_3$ exhibit a half-metallic behavior, further confirming the underestimation of band gaps by the PBE functional.

Furthermore, we observe Li-adsorption-induced valley polarization in the conduction bands at the K and K' points of monolayer $MnPSe_3$, exhibiting a splitting energy of 20.3 meV as shown in Figure 4. The pristine monolayer $MnPSe_3$ possesses an in-plane magnetic moment orientation along the y-direction. When SOC is considered, our calculated band structure (Figure S4) reveals that the valley degeneracy at K and K' points is protected by the combined MT symmetry (where M represents mirror symmetry and T denotes time-reversal symmetry), consistent with the symmetry analysis.[39] The energetically favorable adsorption site for Li atoms is identified at the Mn position, which breaks all mirror symmetry operations. Crucially, our first-principles calculations demonstrate that Li adsorption induces a magnetic easy-axis reorientation from the in-plane to out-of-plane direction (detailed discussion in Section 3.4). This structural modification reduces the magnetic point group symmetry from 2/m′ in the pristine system to 3.1 in the Li-adsorbed system,

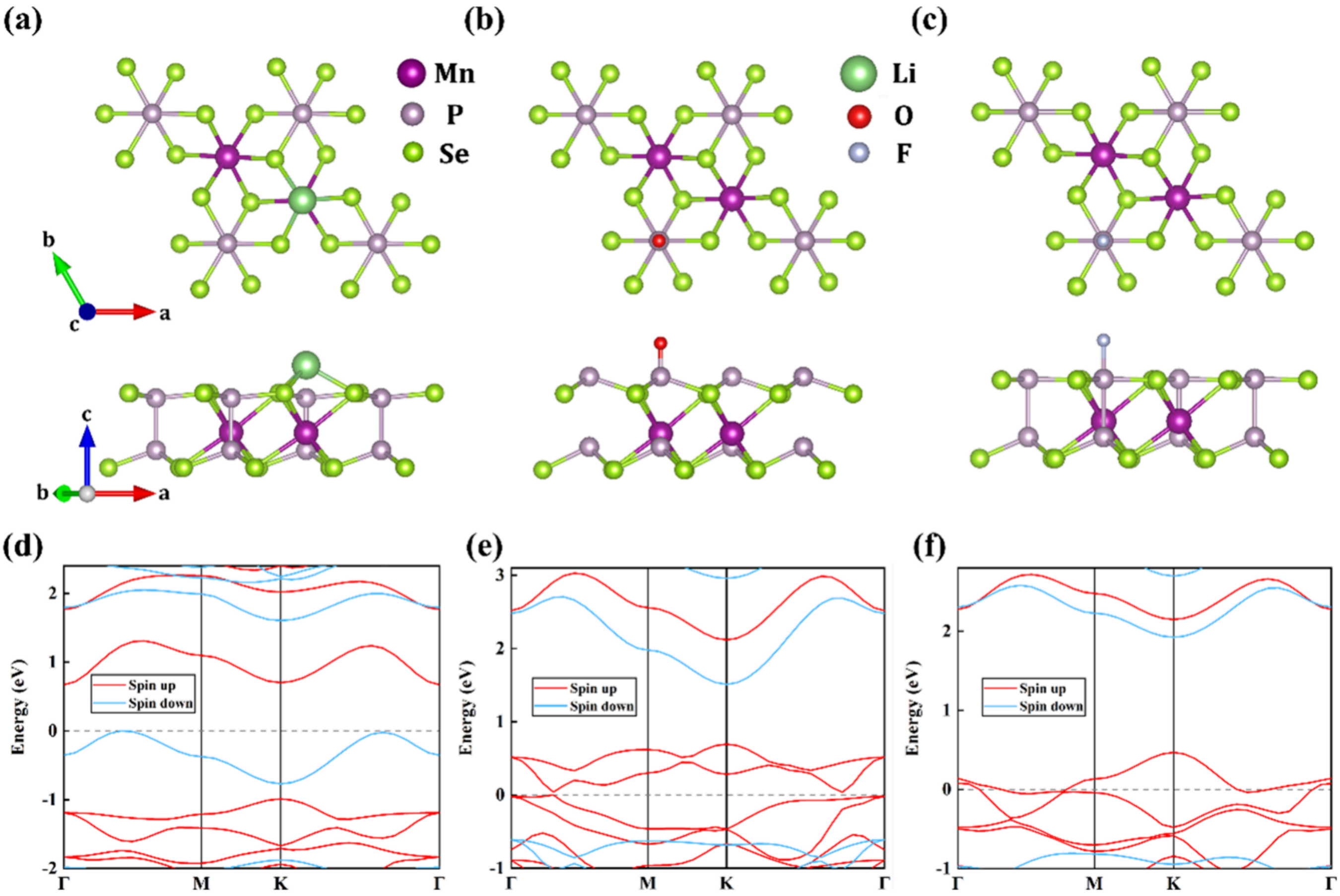

Figure 3. Most energetically favorable configurations with a coverage of 100% after adsorption with the (a) Li atom, (b) O atom, and (c) F atom, along with the corresponding band structures for (d) $Li_{0.5}MnPSe_3$, (e) $O_{0.5}MnPSe_3$, and (f) $F_{0.5}MnPSe_3$. The red and blue solid lines represent the spin-up and spin-down channels, respectively. All of the shown band structures are obtained with the HSE06 functional without SOC.

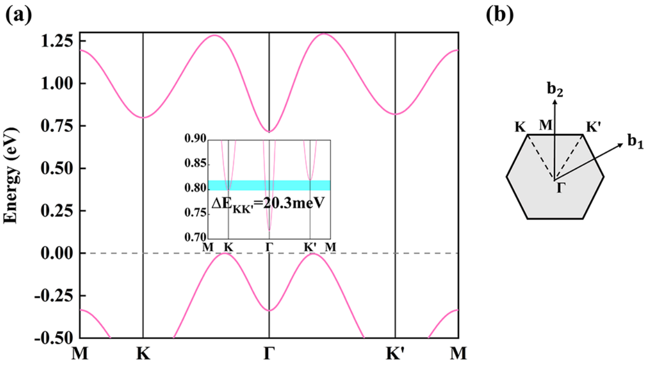

Figure 4. (a) Band structure of $Li_{0.5}MnPSe_3$ calculated using the HSE06 functional with SOC. (b) Corresponding high-symmetry path in the Brillouin zone.

consequently breaking the *MT* symmetry protection. The symmetry-breaking mechanism thereby lifts the valley degeneracy and generates measurable valley polarization under SOC conditions.

The crystal structure after adsorption with differential charge densities is presented in Figure 5, and the electron transfer before and after adsorption is further analyzed using Bader charge calculations. As shown in Figure 5a, the blue region on Li indicates electron depletion, while the yellow region on Se represents electron accumulation. One can see that charges transfer from Li to the surrounding three Se atoms of monolayer $MnPSe_3$ by −0.44 e/f.u. for Li adsorption, resulting in a reduction of the band gap and $MnPSe_3$ gaining electrons. For O and F adsorption, the Bader charge transfers from $MnPSe_3$ to F and O, with transfer amounts of 0.62 and 0.37 e/f.u., respectively, causing the Fermi level to shift downward into $MnPSe_3$, corresponding to hole doping, as shown in Figure 5b,c.

3.4. Adsorbate-Induced Magnetic Modulation.

Next, we calculate the magnetic anisotropy energy (MAE) including SOC to analyze the changes in the easy magnetization axis before and after adsorption. MAE is defined as the total energy difference between $E[001]$ and $E[010]$, i.e., MAE = $E[001] - E[010]$. A positive MAE corresponds to an in-plane magnetization EA, while a negative MAE indicates an out-of-plane magnetization EA. Our calculation results indicate that the magnetic EA of monolayer $MnPSe_3$ lies within the plane and exhibits an in-plane isotropy. To evaluate the MAEs of $Li_{0.5}MnPSe_3$, $MnPSe_3O_{0.5}$, and $MnPSe_3F_{0.5}$, we computed the total energies for different orientations of the magnetic EA using the GGA+*U* method. The influence of *k*-mesh sampling on the MAE was systematically tested, as illustrated in Figure S5.

As shown in Table 2, after Li adsorption, the EA of the entire system shifts from in-plane to out-of-plane, while the adsorption of F and O further increases the magnitude of the MAE.

To describe the 2D magnetic structure, the exchange interaction parameters between Mn^{2+} ion spins were extracted

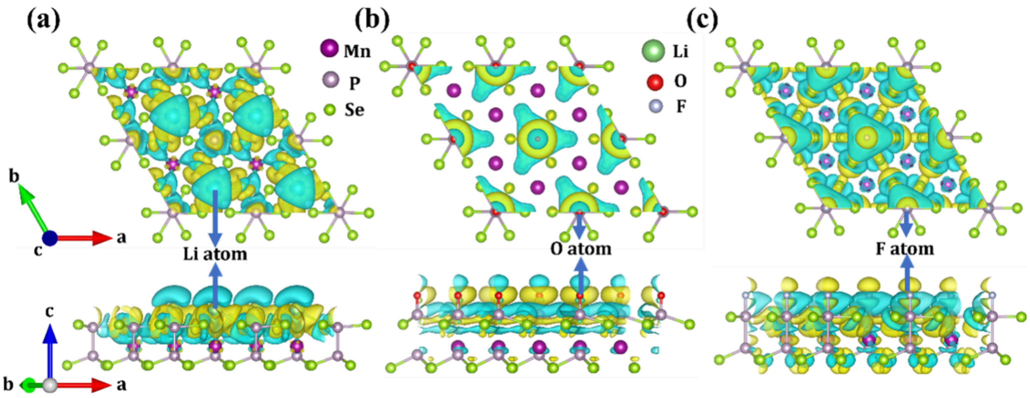

Figure 5. Crystal structures of (a) $Li_{0.5}MnPSe_3$, (b) $O_{0.5}MnPSe_3$, and (c) $F_{0.5}MnPSe_3$ with different charge densities (isovalue 0.001 e × A^{-3}). The blue and yellow distributions correspond to charge depletion and accumulation, respectively.

Table 2. Energy Difference $\Delta E = E(\text{AFM}) - E(\text{FM})$ in meV, and MAE = $E[001] - E[010]$[a]

materials	$MnPSe_3$	$Li_{0.5}MnPSe_3$	$MnPSe_3O_{0.5}$	$MnPSe_3F_{0.5}$
Bader charge (e/f.u.)		−0.44	0.62	0.37
MAE (meV/f.u.)	0.24	−0.27	1.15	0.55
ΔE (meV/f.u.)	−21.9	18.4	76.7	64.2

[a] The Bader charge difference (e/f.u.) is between before and after Li, O, and F adsorption with coverage of 1 ML.

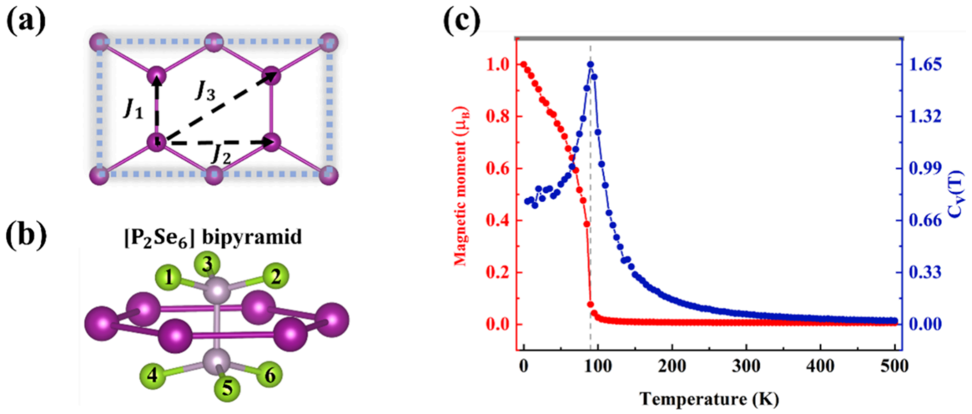

Figure 6. (a) Magnetic exchange parameters J_1, J_2, and J_3 between Mn^{2+} ions. (b) Schematic of the Mn−Se···Se−Mn supersuperexchange pathways governing J_2 and J_3. (c) Simulated magnetic moment μ_B and specific heat C_v with respect to temperature for the pristine $MnPSe_3$ monolayer.

by considering the corresponding anisotropic Heisenberg Hamiltonian:

$$H = \sum_{i,j} J_1\vec{S}_i\vec{S}_j + \sum_{i,j} J_2\vec{S}_i\vec{S}_j + \sum_{i,j} J_3\vec{S}_i\vec{S}_j + A\sum_{i} (S_i^z)^2 \tag{9}$$

where S_i represents the total spin magnetic moment of the atomic site i. J_1, J_2, and J_3 are the exchange interactions between the first, second, and third nearest-neighbor spins, respectively, as shown in Figure 6a. A is the single-ion MAE, and S_i^z is the spin component of the i site along the z direction of the easy magnetization axis. In the pristine monolayer $MnPSe_3$, all of the calculated J values are negative, i.e., $J_1 = -0.45$ meV, $J_2 = -0.04$ meV, and $J_3 = -0.24$ meV, which show an excellent agreement with $J_1 = -0.46$ meV, $J_2 = -0.03$ meV, and $J_3 = -0.19$ meV reported in a previous work.[30] As can be seen in Figure 6c, the Néel temperature of the pristine 2D $MnPSe_3$ is approximately 90 K, which aligns well with previous studies (88 K), thereby validating the reliability of eq 9.[10]

The magnetic ground state of monolayer $MnPSe_3$ is governed by competing exchange interactions, with first- (J_1) and third-nearest-neighbor (J_3) couplings dominating. J_1 arises from the competition between direct exchange and superexchange interactions. The short-range Mn−Mn direct exchange originates from transitions between Mn ions, where the overlapping half-filled 3d-orbitals provide a stable AFM state. Following the Goodenough−Kanamori−Anderson rules, the near-84° Mn−Se−Mn bond angle favors FM superexchange.[40] However, due to the high-spin state of the Mn ions in the monolayer $MnPSe_3$, the direct AFM interaction dominates over the FM superexchange. For J_2 and J_3, the AFM coupling originates from different supersuperexchange pathways mediated by Se atoms. Specifically, J_2 involves the Mn−Se_3···Se_6−Mn channel, which connects Se atoms from different sublayers, while J_3 is associated with the Mn−Se_1···Se_2−Mn interaction mediated by Se atoms within the same sublayer, as shown in Figure 6b.[41] It is reasonable to expect that the hybridization between the Mn-d and Se-p states within the same sublayer is significantly stronger than that between atoms in different sublayers. This explains why J_3 is greater than J_2, despite the longer Mn−Mn distance in the former.

However, J_1 is nearly twice as large as J_3, thereby ensuring AFM ordering in monolayer $MnPSe_3$.

Adsorption of Li, O, and F atoms significantly modulates exchange parameters (see Table S2). Li adsorption reduces the band gap, enhancing Mn−Se−Mn superexchange while increasing Mn−Mn distances to suppress direct exchange. This reverses the J_1 dominance, driving an AFM−FM transition. Similarly, the adsorption of O amplifies next-nearest-neighbor interactions via strengthened *d-p-d* orbital hybridization, inducing a more pronounced exchange parameter shift than Li.

The F atom adsorption-induced AFM−FM transition can be qualitatively explained by the Stoner model. According to the Stoner criterion, ferromagnetism emerges when $D(E_F)J > 1$, where $D(E_F)$ is the DOS at the Fermi level in the nonmagnetic state and J represents the strength of the exchange interaction.[42] The exchange parameter J can be estimated by the ratio of the spin splitting of the electronic states near the Fermi level to the resulting magnetic moment. Specifically, for the $F_{0.5}MnPSe_3$ unit cell, a magnetic moment of 8.9 μ_B is obtained. As illustrated in the Supporting Information, the DOS, $D(E_F)$ is 27.8 states/eV, and the average spin splitting between the first conduction band and the first valence band is 0.55 eV. There, the calculation result confirms that $F_{0.5}MnPSe_3$ satisfies the Stoner criterion ($D(E_F)J > 1$), providing strong evidence that the metallic system exhibits Stoner ferromagnetism.

3.5. MAE Modulation under Carrier Doping.

Subsequently, carrier doping is applied to modulate the electronic and magnetic properties of monolayer $MnPSe_3$. Figure 7 displays the variation of the MAE under carrier doping. A clear trend is observed, where an increase in hole doping concentration leads to an enhancement of the MAE, stabilizing the in-plane EA, while an increase in electron doping concentration continuously decreases the MAE. As the doping concentration reaches a critical threshold, the EA flips from in-plane to out-of-plane. It is clear that the Bader charge induced by the Li adsorption (corresponding to electron doping) exceeds the electron doping mentioned above. To elucidate the origin of the electron-doping-induced reorientation of the magnetic EA from in-plane to out-of-plane, we computed the DOS for both Mn-3*d* and P-3*p* orbitals at electron and hole doping concentrations of 0.5 e/u.c. and 0.5 h/u.c., respectively. As shown in Figure S7, compared with the orbital-projected DOS of pristine monolayer $MnPSe_3$, the energies of the Mn-d_{z^2}, d_{xz}, and d_{yz} orbitals, as well as the P-p_z orbital near the Fermi level, exhibit a noticeable decrease under electron doping at 0.5 e/u.c. In contrast, under hole doping at 0.5 h/u.c., the same orbitals show a significant increase in energy around the Fermi level. These shifts lead to an enhancement in the MAE, further stabilizing the in-plane magnetic axis in the hole-doped case.

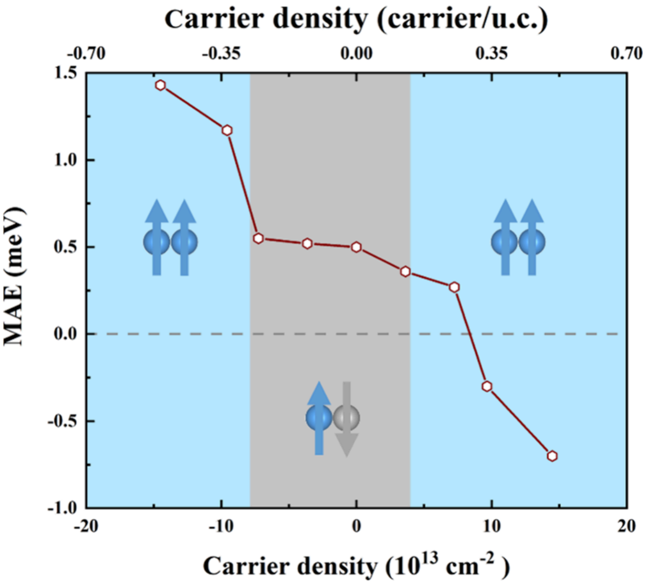

Figure 7. Variation of MAE (MAE = E[001] − E[010]) with carrier doping concentration. The blue region represents the FM ground state, while the gray region corresponds to the AFM ground state.

According to previous studies, the reorientation of the magnetic EA from in-plane to out-of-plane alters the magnetic space group of $MnPSe_3$ from $2'/m$ to $\bar{3}'$ m.[35]. This symmetry breaking lifts the valley degeneracy at the *K* and *K′* points in the Brillouin zone and can induce valley polarization in the presence of SOC. Therefore, it is reasonable to expect that electron doping serves as an effective route to realize valley polarization in monolayer $MnPSe_3$.

Moreover, through comprehensive consideration of multiple AFM configurations (Néel-AFM, zigzag-AFM, stripy-AFM), we serendipitously discovered that the phase transition critical concentration (8×10^{13} cm^{-2} for holes and 4.5×10^{13} cm^{-2} for electrons) in monolayer $MnPSe_3$ actually surpasses the value reported in a previous study.[10] This discrepancy arises from the competitive energy stabilization mechanism, where alternative AFM configurations (stripy-AFM and zigzag-AFM) may preferentially occupy lower-energy states under specific doping conditions.

4. CONCLUSIONS

In summary, we have established atomic adsorption as a transformative strategy for tailoring magnetic order and electronic states in monolayer $MnPSe_3$, addressing critical challenges in 2D spintronic and valleytronic material design. Adsorption energy calculations for Li, O, and F at various coverages indicate that the low-coverage adsorption configurations are intrinsically unstable. Instead, these species exhibit a spontaneous tendency to aggregate, leading to the formation of regions with locally high adsorption coverage. Phase diagrams under equilibrium conditions reveal enhanced thermodynamic stability at high coverages. Furthermore, HSE06 calculations demonstrate that full-coverage Li/O adsorption reduces the band gap, amplifying *d-p-d* superexchange interactions to drive AFM−FM transitions, while F adsorption induces a Stoner ferromagnetism via the half-metallic band structure, evidenced by the Stoner criterion ($D(E_F)J > 1$). Li adsorption not only reorients the magnetic EA of monolayer $MnPSe_3$ from in-plane to out-of-plane but also induces valley polarization (∼20.3 meV) at the *K*/*K′* points of the Brillouin zone, demonstrating concurrent control over spin and valley degrees of freedom. Crucially, carrier doping results indicate that when the electron doping concentration reaches 8.3×10^{13} cm^{-2}, the magnetic EA of monolayer $MnPSe_3$ reorients from an in-plane to an out-of-plane configuration, while the magnitude of the in-plane MAE increases with higher hole doping levels. These insights redefine design principles for 2D magnetic semiconductors by emphasizing the synergy between thermodynamics and spin dynamics. The coverage−stability−magnetism triad delineated herein provides a universal framework for engineering interfacial phenomena in 2D adsorption systems, thereby advancing their integration into nonvolatile spintronic memory and logic architectures.

■ ASSOCIATED CONTENT

Supporting Information

The Supporting Information is available free of charge at https://pubs.acs.org/doi/10.1021/acs.jpcc.5c04044.

> Band structures of monolayer $MnPSe_3$ under various Hubbard U values; optimized atomic configurations for adatoms at different coverages; GGA+U band structures for $Li_{0.5}MnPSe_3$ and $MnPSe_3Li_{0.5}$; SOC-included band structure of $Li_{0.5}MnPSe_3$; MAE convergence with k-mesh; Stoner criterion for $MnPSe_3F_{0.5}$; magnetic exchange parameters for pristine $MnPSe_3$, $Li_{0.5}MnPSe_3$, $MnPSe_3O_{0.5}$, and $MnPSe_3F_{0.5}$; and PDOS of pristine, 0.5 e/u.c., and 0.5 h/u.c. doped $MnPSe_3$ (PDF)

■ AUTHOR INFORMATION

Corresponding Author

Yu-Jun Zhao − *Department of Physics, South China University of Technology, Guangzhou 510640, China;* orcid.org/0000-0002-6923-1099; Email: zhaoyj@scut.edu.cn

Authors

Dong Liu − *Department of Physics, South China University of Technology, Guangzhou 510640, China*

Sike Zeng − *Department of Physics, South China University of Technology, Guangzhou 510640, China*

Ji-Hai Liao − *Department of Physics, South China University of Technology, Guangzhou 510640, China*

Complete contact information is available at: https://pubs.acs.org/10.1021/acs.jpcc.5c04044

Notes

The authors declare no competing financial interest.

■ ACKNOWLEDGMENTS

The authors gratefully acknowledge Professor Xiao-Bao Yang for insightful discussions regarding the Stoner criterion calculations for $MnPSe_3F_{0.5}$. This work was supported by the Guangdong Basic and Applied Basic Research Foundation (No. 2023A1515012289) and the National Natural Science Foundation of China (Grant No. 12474229). This work was partially supported by the High Performance Computing Platform of South China University of Technology.

■ REFERENCES

(1) Novoselov, K. S.; Geim, A. K.; Morozov, S. V.; Jiang, D.; Zhang, Y.; Dubonos, S. V.; Grigorieva, I. V.; Firsov, A. A. Electric field effect in atomically thin carbon films. *Science* **2004**, *306*, 666.

(2) Geim, A. K.; Novoselov, K. S. The rise of graphene. *Nat. Mater.* **2007**, *6*, 183.

(3) Castro Neto, A. H.; Guinea, F.; Peres, N. M. R.; Novoselov, K. S.; Geim, A. K. The electronic properties of graphene. *Rev. Mod. Phys.* **2009**, *81*, 109.

(4) Mermin, N. D.; Wagner, H. Absence of Ferromagnetism or Antiferromagnetism in One- or Two-Dimensional Isotropic Heisenberg Models. *Phys. Rev. Lett.* **1966**, *17*, 1133.

(5) Gong, C.; Li, L.; Li, Z.; Ji, H.; Stern, A.; Xia, Y.; Cao, T.; Bao, W.; Wang, C. Z.; Wang, Y.; et al. Discovery of intrinsic ferromagnetism in two-dimensional van der Waals crystals. *Nature* **2017**, *546*, 265.

(6) Huang, B.; Clark, G.; Navarro-Moratalla, E.; Klein, D. R.; Cheng, R.; Seyler, K. L.; Zhong, D.; Schmidgall, E.; McGuire, M. A.; Codben, D. H.; et al. Layer-dependent ferromagnetism in a van der Waals crystal down to the monolayer limit. *Nature* **2017**, *546*, 270.

(7) Deng, Y.; Yu, Y.; Song, Y.; Zhang, J.; Wang, N. Z.; Sun, Z.; Yi, Y.; Wu, Y. Z.; Wu, S.; Zhu, J.; et al. Gate-tunable room-temperature ferromagnetism in two-dimensional Fe_3GeTe_2. *Nature* **2018**, *563*, 94.

(8) Mounet, N.; Gibertini, M.; Schwaller, P.; Campi, D.; Merkys, A.; Marrazzo, A.; Sohier, T.; Capellotti, I. E.; Pizzi, G.; et al. Two-dimensional materials from high-throughput computational exfoliation of experimentally known compounds. *Nat. Nanotechnol.* **2018**, *13*, 246.

(9) de Groot, R. A.; Mueller, F. M.; van Engen, P. G.; Buschow, K. H. J. New Class of Materials: Half-Metallic Ferromagnets. *Phys. Rev. Lett.* **1983**, *50*, 2024.

(10) Li, X.; Wu, X.; Yang, J. Half-Metallicity in $MnPSe_3$ Exfoliated Nanosheet with Carrier Doping. *J. Am. Chem. Soc.* **2014**, *136*, 11065.

(11) Lin, X.; Yang, W.; Wang, K. L.; Zhao, W. Two-dimensional spintronics for low-power electronics. *Nature Electronics* **2019**, *2*, 274.

(12) Sierra, J. F.; Fabian, J.; Kawakami, R. K.; Roche, S.; Valenzuela, S. O. Van der Waals heterostructures for spintronics and opto-spintronics. *Nat. Nanotechnol.* **2021**, *16*, 856.

(13) Yu, S.; Tang, J.; Wang, Y.; Xu, F.; Li, X.; Wang, X. Recent advances in two-dimensional ferromagnetism: strain-, doping-, structural- and electric field-engineering toward spintronic applications. *Sci. Technol. Adv. Mater.* **2022**, *23*, 140.

(14) Xian, J.-J.; Wang, C.; Nie, J.-H.; Li, R.; Han, M.; Lin, J.; Zhang, W.-H.; Liu, Z.-Y.; Zhang, Z.-M.; Miao, M.-P.; et al. Spin mapping of intralayer antiferromagnetism and field-induced spin reorientation in monolayer CrTe2. *Nat. Commun.* **2022**, *13*, 257.

(15) Gao, P.; Li, X.; Yang, J. Thickness Dependent Magnetic Transition in Few Layer 1T Phase CrTe2. *J. Phys. Chem. Lett.* **2021**, *12*, 6847.

(16) Wang, N.; Chen, J.; An, Y.; Zhan, Q.; Gong, S.-J. Controllable half-metallicity in MnPX3 monolayer. *npj Spintron.* **2024**, *2*, 60.

(17) Zhang, Y.; Zhang, Y.; Ye, H.; Zhang, J.; Wang, J. Transition from antiferromagnetic metal to room-temperature ferromagnetic semiconductor in monolayer CrTe2 via Li adsorption. *Phys. Rev. B* **2024**, *109*, No. 195426.

(18) Gao, Y.; Jiang, X.; Qiu, Z.; Zhao, J. Photoexcitation induced magnetic phase transition and spin dynamics in antiferromagnetic MnPS3 monolayer. *npj Comput. Mater.* **2023**, *9*, 107.

(19) Guan, Z.; Ni, S.; Hu, S. First-Principles Study of 3d Transition-Metal-Atom Adsorption onto Graphene Embedded with the Extended Line Defect. *ACS omega* **2020**, *5* (11), 5900−5910.

(20) Wang, K.; Ren, K.; Hou, Y.; Cheng, Y.; Zhang, G. Physical insights into enhancing magnetic stability of 2D magnets. *J. Appl. Phys.* **2023**, *133*, 110902.

(21) Wiedenmann, A.; Rossat-Mignod, J.; Louisy, A.; Brec, R.; Rouxel, J. Neutron diffraction study of the layered compounds MnPSe3 and FePSe3. *Solid State Commun.* **1981**, *40*, 1067.

(22) Gillard, D. J.; Wolverson, D.; Hutchings, O. M.; Tartakovskii, A. I. Spin-order-dependent magneto-elastic coupling in two dimensional antiferromagnetic MnPSe3 observed through Raman spectroscopy. *npj 2D Mater. Appl.* **2024**, *8*, 6.

(23) Mazin, I.; González-Hernández, R.; mejkal, L. Š. Induced Monolayer Altermagnetism in MnP(S,Se)3 and FeSe. *arXiv* **2023**.

(24) Wang, B.-J.; Sun, Y.-Y.; Chen, J.; Ju, W.; An, Y.-P.; Gong, S.-J. Valley splitting in the antiferromagnetic heterostructure MnPSe3/WSe2. *J. Mater. Chem. C* **2021**, *9*, 3562.

(25) Dong, X.; Jia, K.; Ji, W.; Li, S.; Zhang, C.-W. Realization of Dual Anomalous Valley Hall Effect in Antiferromagnetic HfN2/MnPSe3 Heterostructure. *ACS Appl. Electron. Mater.* **2024**, *6*, 679.

(26) Perdew, J. P.; Burke, K.; Ernzerhof, M. Generalized Gradient Approximation Made Simple. *Phys. Rev. Lett.* **1996**, *77*, 3865.

(27) Kresse, G.; Furthmüller, J. Efficient iterative schemes for ab initio total-energy calculations using a plane-wave basis set. *Phys. Rev. B* **1996**, *54*, 11169.

(28) Heyd, J.; Scuseria, G. E.; Ernzerhof, M. Hybrid functionals based on a screened Coulomb potential. *J. Chem. Phys.* **2003**, *118*, 8207.

(29) Wang, X.; Wang, D.; Wu, R.; Freeman, A. J. Validity of the force theorem for magnetocrystalline anisotropy. *J. Magn. Magn. Mater.* **1996**, *159*, 337.

(30) Sivadas, N.; Daniels, M. W.; Swendsen, R. H.; Okamoto, S.; Xiao, D. Magnetic ground state of semiconducting transition-metal trichalcogenide monolayers. *Phys. Rev. B* **2015**, *91*, No. 235425.

(31) Li, J.; Li, Y.; Du, S.; Wang, Z.; Gu, B.-L.; Zhang, S.-C.; He, K.; Duan, W.; Xu, Y. Intrinsic magnetic topological insulators in van der Waals layered MnBi2Te4-family materials. *Sci. Adv.* **2019**, *5*, No. eaaw5685.

(32) An, Y.; Wang, K.; Gong, S.; Hou, Y.; Ma, C.; Zhu, M.; Zhao, C.; Wang, T.; Ma, S.; Wang, H.; et al. Nanodevices engineering and spin transport properties of MnBi_2 Te_4 monolayer. *npj Comput. Mater.* **2021**, *7*, 45.

(33) Wu, H.; Burnus, T.; Hu, Z.; Martin, C.; Maignan, A.; Cezar, J. C.; Tanaka, A.; Brookes, N. B.; Khomskii, D. I.; Tjeng, L. H. Ising Magnetism and Ferroelectricity in Ca3Co MnO6. *Phys. Rev. Lett.* **2009**, *102*, No. 026404.

(34) https://vampire.york.ac.uk/.

(35) Evans, R. F. L.; Fan, W. J.; Chureemart, P.; Ostler, T. A.; Ellis, M. O. A.; Chantrell, R. W. Atomistic spin model simulations of magnetic nanomaterials. *J. Phys.: Condens. Matter* **2014**, *26*, No. 103202.

(36) Yang, J.; Zhou, Y.; Guo, Q.; Dedkov, Y.; Voloshina, E. Electronic, magnetic and optical properties of MnPX3 (X = S, Se) monolayers with and without chalcogen defects: a first-principles study. *RSC Adv.* **2020**, *10*, 851.

(37) Chittari, B. L.; Park, Y.; Lee, D.; Han, M.; MacDonald, A. H.; Hwang, E.; Jung, J. Electronic and magnetic properties of single-layer MPX3 metal phosphorous trichalcogenides. *Phys. Rev. B* **2016**, *94*, No. 184428.

(38) Du, K.; Wang, X.; Liu, Y.; Hu, P.; Utama, M. I. B.; Gan, C. K.; Xiong, Q.; Kloc, C. Weak Van der Waals Stacking, Wide-Range Band Gap, and Raman Study on Ultrathin Layers of Metal Phosphorus Trichalcogenides. *ACS Nano* **2016**, *10*, 1738.

(39) Xue, Q.; Mu, X.; Sun, Y.; Zhou, J. Valley contrasting bulk photovoltaic effect in a PT-symmetric MnPSe3 monolayer. *Phys. Rev. B* **2023**, *107*, No. 245404.

(40) Kanamori, J. Superexchange interaction and symmetry properties of electron orbitals. *J. Phys. Chem. Solids* **1959**, *10*, 87.

(41) Pei, Q.; Wang, X.-C.; Zou, J.-J.; Mi, W.-B. Tunable electronic structure and magnetic coupling in strained two-dimensional semiconductor MnPSe3. *Front. Phys.* **2018**, *13*, 137105.

(42) Stoner, E. C. Collective electron ferromagnetism. *Proc. R. Soc. A* **1938**, *165*, 372.

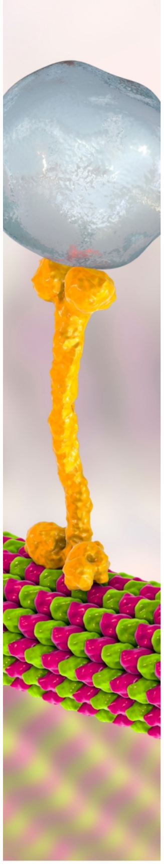

https://doi.org/10.1021/acs.jpcc.5c04044
J. Phys. Chem. C 2025, 129, 17287−17295